Small extracellular vesicles with nanomorphology memory promote osteogenesis

Liang Ma [a,1], Wencan Ke [a,1], Zhiwei Liao [a,1], Xiaobo Feng [a,1], Jie Lei [a], Kun Wang [a], Bingjin Wang [a], Gaocai Li [a], Rongjin Luo [a], Yunsong Shi [a], Weifeng Zhang [a], Yu Song [a,**], Weibin Sheng [b,***], Cao Yang [a,*]

[a] Department of Orthopaedics, Union Hospital, Tongji Medical College, Huazhong University of Science and Technology, Wuhan, 430022, China
[b] Department of Spine Surgery, The First Affiliated Hospital of Xinjiang Medical University, Urumqi, 830054, China

A B S T R A C T

Nanotopographical cues endow biomaterials the ability to guide cell adhesion, proliferation, and differentiation. Cellular mechanical memory can maintain the cell status by retaining cellular information obtained from past mechanical microenvironments. Here, we propose a new concept "morphology memory of small extracellular vesicles (sEV)" for bone regeneration. We performed nanotopography on titanium plates through alkali and heat (Ti8) treatment to promote human mesenchymal stem cell (hMSC) differentiation. Next, we extracted the sEVs from the hMSC, which were cultured on the nanotopographical Ti plates for 21 days (Ti8-21-sEV). We demonstrated that Ti8-21-sEV had superior pro-osteogenesis ability *in vitro* and *in vivo*. RNA sequencing further confirmed that Ti8-21-sEV promote bone regeneration through osteogenic-related pathways, including the PI3K-AKT signaling pathway, MAPK signaling pathway, focal adhesion, and extracellular matrix-receptor interaction. Finally, we decorated the Ti8-21-sEV on a 3D printed porous polyetheretherketone scaffold. The femoral condyle defect model of rabbits was used to demonstrate that Ti8-21-sEV had the best bone ingrowth. In summary, our study demonstrated that the Ti8-21-sEV have memory function by copying the pro-osteogenesis information from the nanotopography. We expect that our study will encourage the discovery of other sEV with morphology memory for tissue regeneration.

1. Introduction

Large-sized bone defects can severely reduce the quality of life of individuals [1–3]. The preferred treatment is autogenous bone, which is regarded as the gold standard by clinicians [4,5]. However, the limited availability of the autografts and the morbidity of the donor site of patients restricts their wide usage [6]. Synthetic bone substitutes combined with bioactive factors or human bone marrow mesenchymal stem cells (hMSC) can enhance the repair efficacy. However, the use of hMSC has several limitations, including immune rejection, undirected cell differentiation, and low survival rate [2,7].

In recent years, the use of three-dimensional (3D) printing scaffolds to promote bone regeneration has attracted considerable attention due to its customizable structures and desirable properties [8,9]. Polyetheretherketone (PEEK) has appropriate mechanical properties with much lower elastic modulus than titanium (Ti) (3–4 GPa versus 102–110 GPa), which can avoid the stress-shielding effect [10,11]. Moreover, PEEK is radiolucent and produces no artifacts when compared with metallic implants [12]. Owing to the above advantages, PEEK is currently considered an alternative material for Ti and its alloys [13], and PEEK related materials are being increasingly applied in clinical practice for various purposes such as hip joint prostheses [14], intervertebral fusion device [15], and dental implants [16]. However, PEEK materials are highly hydrophobic, which reduces cell adhesion

and bioinertness, thereby limiting bone tissue regeneration and causing loosening or even premature failure of the implants [17,18]. Different methods have been used to modify PEEK to enhance the biomechanical compatibility of the PEEK scaffold. For example, Torstrick et al. compared the porous PEEK with plasma-sprayed titanium coated PEEK, and concluded that the porous PEEK had superior osteogenic differentiation and osseointegration ability than smooth PEEK. In addition, the radiolucent characteristic of porous PEEK enabled the direct observation of bone ingrowth through μCT [19]. He et al. combined PEEK with graphene nanosheets to achieve bone tissue regeneration [20]. Yan et al. incorporated CuO/Ag micro/nano particles into porous PEEK through polydopamine and silk, and Cu^{2+} and Ag^+ were released through pH-control to enhance bone regeneration [21]. However, most of those approaches mainly focused on adding bioactive materials such as cytokines, nanomaterials containing metal ions, and stem cells, which the security is controversial.

The small extracellular vesicle (sEV) originates from a nano-sized (30–150 nm) endocytic pathway [22]. Intercellular communication through sEV is a crucial process for tissue progression [23]. The sEV can transfer its encapsulated bioactive components such as RNA, proteins, and lipids to regulate cellular behavior [24].

Physical topographical cues such as the macroscale, microscale, and nanoscale characteristics of biomaterials exert a profound influence on the regulation of cell response, including adhesion, proliferation, and differentiation [25,26]. Recently, Doloff et al. examined the immune-related complications such as foreign body response and capsular fibrosis of clinically approved breast implants, which have a different surface topography, and they concluded that the breast implants with an average roughness of 4 μm can largely suppress the immune-related complications and provoke the least amount of inflammation [27]. Hu et al. evaluated the effects of three types of surface topographies of electrospun membranes on wound healing and immunomodulatory properties. They revealed diverse immune cellular heterogeneity through single-cell RNA sequencing [28]. The above studies indicate that the physical topographical features significantly affect the behavior of cells. In addition, nanomorphology has a greater influence on osseointegration. For example, Yao et al. prepared nanoflake structures through hydrothermal treatment of Ti, and demonstrated that the nanostructure has superior osteogenesis [29]. Bai et al. studied the influence of the nanosurface characteristic on the blood clot property and inflammatory reaction in bone regeneration, and concluded that a titania nanotube with a diameter of 15 nm facilitates bone regeneration by manipulating a favorable osteoimmunomodulatory environment [30].

Recent studies have emphasized the importance of "mechanical memory" of the cell. "Mechanical memory" means that the cell retains information from past mechanical microenvironments [31]. For example, a rigid substrate induced human mesenchymal stem cells to override the soft signal, and a soft substrate encouraged osteogenic differentiation, which usually primed adipogenic differentiation [32]. Li et al. demonstrated that MSC acquired mechanical memory of myofibroblast through cultured on pathophysiologically stiff or soft substrates. Although changed the subsequent mechanical stimulus. MSC still retained the past information for at least two passages, in addition, MSCs transplanted from soft substrates enhance wound quality [33]. All the above studies indicate that mechanical microenvironment has an important effect on cells.

In this study, we demonstrated a new concept "morphology memory of sEV" for bone defect treatment. "Morphology memory of sEV" means that the sEV secreted from cells retain the cellular delivery information on biomaterials with specific morphological characteristics. First, we applied a specific nanomorphology on Ti, which was capable of promoting hMSC differentiation. Next, we extracted the sEV from cells cultured on nanomorphologic scaffolds for 21 days (Ti8-21-sEV). We demonstrated that Ti8-21-sEV had the ability to promote osteogenesis *in vitro* and *in vivo*. Finally, RNA sequencing further confirmed that Ti8-21-

sEVs promote bone regeneration through certain osteogenic pathways (Fig. 1).

2. Materials and methods

2.1. Sample preparation and characterization

Commercial Ti plates (purity >99%) with different nanotopography designs were fabricated through alkali and heat treatment. The Ti plates were successively polished using SiC papers (240, 400, 800, and 1200 grids). Next, the polished Ti plates were cleaned through sequential ultrasonication with acetone, ethanol, and DI water. Then, the Ti samples were immersed in 8 M NaOH at 80 °C for 2 h; this sample was named Ti8, and unprocessed polished titanium plates were set as the control group. Finally, the Ti8 plates were washed with ethanol and water three times.

The characterization of the Ti and Ti8 surface morphologies was performed through field-emission SEM (ZEISS Sigma 500). The surface roughness was examined using an AFM device (Solver Nano, NT-MDT, Russia) in the tapping mode. The wettability of the different samples was measured through a contact angle goniometer (JC2000D2, Power-ach, China).

2.2. Cell culture

Human bone marrow mesenchymal stem cells (hMSC) were isolated from the bone marrow of patients undergoing joint replacement after obtaining signed informed consent. The cells were incubated in a growth medium with 15% fetal bovine serum added with 1% penicillin-streptomycin in a cell incubator with 5% CO_2 at 37 °C. The cell supernatant was changed every three days. The cells were digested through 0.05% trypsin−EDTA.

2.3. Cell morphology on different Ti plates

The hBMSCs were grown on Ti or Ti8 plates. After culturing for 24 h, the cells were fixed with 2.5% glutaraldehyde for 25 min. Then, we used ethanol of different concentrations (15%, 30%, 50%, 75%, 95%, and 100%) for gradient dehydration. Next, gold was sprayed on the plates for 120 s, and the cell morphology was observed through SEM (Zeiss Sigma 500, Germany). The cell spreading area and cell aspect ratio were calculated using ImageJ software according to the SEM images. To observe the cytoskeleton, the cells were fixed with 2.5% glutaraldehyde for 25 min before using phalloidin to reveal F-actin and DAPI to reveal the nucleus.

2.4. Cell viability

The viability of hBMSCs cultured on the different Ti samples were examined using the Cell Counting Kit-8 (CCK-8, Dojindo, Japan). In brief, 3×10^4 hMSC were seeded on different Ti samples pre-placed in 24-well plates. After 1, 3, and 5 days of incubation, CCK-8 reagent was added according to the instructions. The samples were washed three times with PBS, and 10% CCK-8 working solution was added into each well. Then, the samples were incubated at room temperature in dark for 3 h. Finally, we extracted 100 μL of the solution from each well and added it to a new 96-well plate. The cell viability was measured based on the optical density (OD) at the wavelength of 450 nm.

2.5. Live/dead cell staining

The viability of the cells cultured on Ti and Ti8 was further quantified by calcein-AM/PI (Dojindo, Japan). The Ti group was denoted as the control. The cells were first rinsed with PBS three times, and then cultured with 2 μmol/L calcein-AM and 4 μmol/L propidium iodide (PI) for 15 min at 37 °C under dark conditions. Finally, the live and dead cells
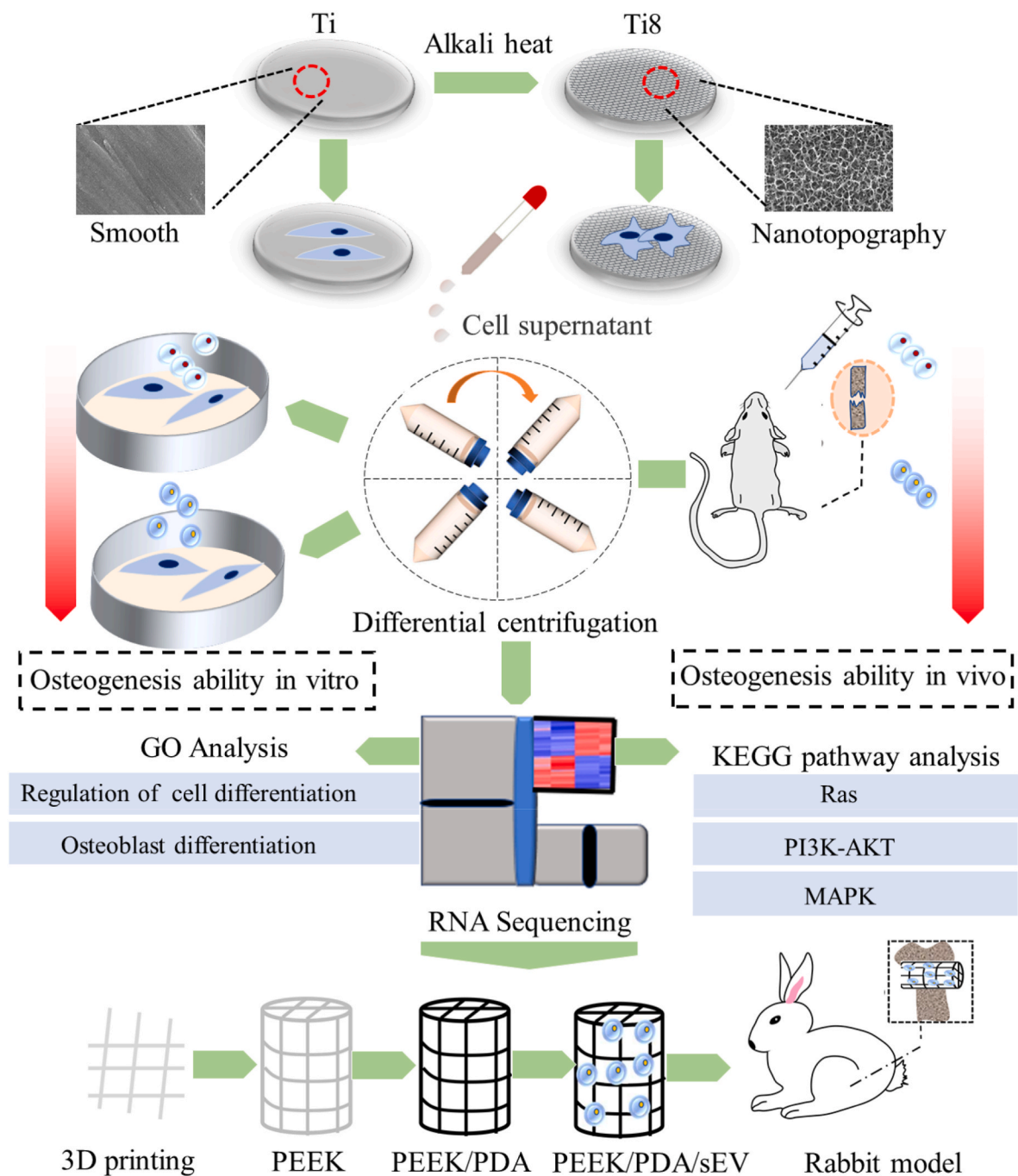
Fig. 1. Scheme illustration of small extracellular vesicles with nanomorphology memory promote osteogenesis.

were observed through a fluorescence microscope (Olympus IX71, Tokyo, Japan).

2.6. Alizarin red staining (ARS) and quantification

The osteogenic differentiation ability of the cells was measured using ARS. The hMSC were washed with PBS before fixing with 4% formaldehyde for 25 min. Then, the cells were washed with PBS and 1% Alizarin red was used to stain the cells for 30 min. Finally, the calcium nodules were observed through an inverted microscope. To quantitative analyze the mineralized nodules, 10% hexadecyl pyridinium chloride was incubated with the cells, and measured through a microplate reader at 562 nm.

2.7. Alkaline phosphatase (ALP) staining and activity measurement

The osteogenic differentiation ability was further measured through ALP staining and quantitative analysis. For the ALP staining, the cells were fixed with 4% formaldehyde for 25 min. Then, the cells were stained with BCIP/NBT Kit (Beyotime, China) and the images were observed through an inverted microscope. In addition, an alkaline phosphatase assay kit (Nanjing Jiancheng Bioengineering Institute, China) was used for the quantitative analysis of ALP and the total amount of protein was determined using a bicinchoninic acid (BCA) protein assay kit (Boster Biological Technology Co., Ltd., China). The quantitative result was then calculated based on the ALP content and total protein content according to the manufacturer's guidance.

2.8. RNA extraction and quantitative reverse-transcription polymerase chain reaction (qRT-PCR)

Total RNA was extracted from the hMSC by using a trizol reagent (Invitrogen). Then, the RNA concentration was obtained by utilizing the NanoDrop spectrophotometer (Thermo Fisher Scientific, Waltham, MA, USA). The extracted RNA was reverse-transcribed using a cDNA synthesis kit (TaKaRa, Japan) followed by qRT-PCR using RT SuperMix for qPCR (TaKaRa, Japan). The results were calculated with the $2^{-\Delta\Delta}$ CT method normalized to GAPDH. The primers used in our study are listed in Table S1.

2.9. Isolation of hMSC-derived sEV

The hMSCs were cultured with exosome depleted fetal bovine serum which purchase from Shanghai XP Biomed Ltd, and the supernatant was collected. Then, the sEV were isolated through a differential centrifugation method. First, the cell debris was removed through low-speed centrifugation at 300g and 2000 g for 20 min. Then, centrifugation at 10,000 g was used to remove the large extracellular vesicles (500–1000 nm). Finally, centrifugation at 100,000 g was used for 70 min to precipitate the sEV. The EVs were resuspended in 100 μL PBS and stored at −80 °C. The protein concentration in the EV was determined using the BCA protein analysis kit.

2.10. Transmission electron microscopy (TEM)

The size of the sEV was measured through transmission electron microscopy (TEM). The sEV were fixed with 2.5% glutaraldehyde for 25 min and incubated on a carbon-coated copper grid for 15 min. Then, 1% uranyl acetate solution was used to stain the samples for 2 min at room temperature. Finally, the sEV images were obtained using transmission electron microscopy (FEI Tecnai G20 TWIN, USA). The size of the sEV was measured using a NANOSIGHT NS300 system (Malvern, UK). The results were analyzed using the NTA software.

2.11. Western blot assay

The markers of sEV, namely, CD9 (Abcam) and CD63 (Abcam), were identified through western blotting assay. The protein content was measured using a BCA protein assay kit. Then, the proteins of the cells and sEV of equivalent amounts were separated on a 10% SDS-PAGE gel and transferred to 0.22 μm PVDF membranes. Finally, the membrane was visualized by using an enhanced chemiluminescence system (Bio-Rad).

2.12. sEV internalization experiments

We first incubated the cells with PKH26 (Sigma-Aldrich) labeled sEV for 24 h. Then, the cells were fixed with 4% paraformaldehyde for 25 min and DAPI was used to label the nucleus. Finally, a microscope (Olympus, Japan) was used to observe the PKH26-sEV internalization.

2.13. Immunofluorescence (IF)

The hMSC were seeded on slides and incubated with 50 μg/mL control-sEV, Ti-21-sEV, and Ti8-21-sEV for 3 days. The sEV secreted from hMSC, which were cultured on a cell culture dish, were denoted as the control. After 7 days, the cells were fixed with 4% paraformaldehyde for 25 min and washed with PBS three times. Then, the cells were permeabilized with 0.2% Triton X-100 and blocked with bovine serum albumin for 30 min before incubating overnight at 4 °C with primary antibodies such as RUNX2 (Abcam), OCN (Abcam), and ALP (Abcam). Furthermore, fluorescent-conjugated secondary antibodies were incubated with the cells for 1 h, and F-actin was stained with FITC-phalloidin. The nuclei were stained using 4-6-diamidino-2-phenylindole

(DAPI, Beyotime Biotechnology, China) for 5 min. Finally, the images were observed through a fluorescence microscope (Olympus, BX53; Melville, NY, USA). The fluorescence intensity was calculated using ImageJ (National Institute of Health, USA).

2.14. Mice femoral fracture model and sEV treatment

A total of 60 Mice (10 W C57BL/6J; male) were obtained from the Institute of Laboratory Animal Science of Huazhong University of Science and Technology (Wuhan, China). All animal studies were approved by the Animal Experimentation Committee of Huazhong University of Science and Technology (Wuhan, China). To construct the mice fracture model, we first administered intraperitoneal anesthesia to the mice using 1% pentobarbital sodium. The right femoral middle segment fracture was constructed using a diamond disk and 23-gauge syringe needle to stabilize the fracture and four mice died during surgery. On the second day after surgery, 50 μg/mL, 200 μL PBS, Ti-21-sEV, and Ti8-21-sEV were injected at the fracture site for five consecutive days and the group injected with PBS was denoted as the control group. The femur specimens were collected after 14 days and 21 days for follow-up experiments.

2.15. RNA sequencing

RNA sequencing was conducted after culturing hMSC with Ti-21-sEV and Ti8-21-sEV for 21 days. we used the stem cells from same person of P2, and we did not add osteogenic induction medium. Cells that did not receive any treatment were the control group, denoted as A; cells incubated with Ti-21-sEV were denoted as B, and cells incubated with Ti-21-sEV were denoted as C. RNA sequencing was repeated three times for each group. The total RNA was isolated using TRIzol reagent (Invitrogen, Carlsbad, CA, USA). One microgram of RNA per sample was used as the input material for RNA sample preparation. We used NEBNext® Ultra™ RNA Library Prep Kit (Illumina, NEB, United States) as the sequencing library.

After quality assessment, the library preparations were sequenced on an Illumina Hiseq platform. Differential expression analysis was selected with fold change >|2| and p value < 0.05. GO enrichment and KEGG were used to identify the potential pathways.

2.16. Fabrication and modification of 3D-printed PEEK scaffold

PEEK scaffolds of 5 mm diameter and 10 mm height were fabricated layer-by-layer through fused deposition modeling (FDM) by using PEEK filament from Evonik Industries AG (Germany) with diameter of 1.75 mm. To decorate Ti8-21-sEV on the PEEK scaffolds, the scaffolds were firstly coated with PDA by immersing them in 2 mg/mL dopamine solution (10 mM Tris-HCl, pH 8.5, Sigma-Aldrich, St. Louis, MO) and shaking for 24 h at 37 °C. Then, the scaffolds were washed three times in an ultrasonic cleaner with distilled water to remove the unattached dopamine, and subsequently sterilized in 75% ethanol and washed with PBS. Finally, the PEEK/PDA scaffolds were immersed in 50 μg/mL sEV solution for 24 h at 4 °C.

2.17. In vivo imaging system

In vivo fluorescence imaging of the PEEK scaffolds and PEEK/PDA/sEV scaffolds was performed. PEEK and PEEK/PDA/sEV were placed into the skin on the right and left side of the body of C57BL/6J mice, respectively. After 1, 3, 5, 7 days, the mice were imaged with an FX PRO imaging system (BRUKER, Karlsruhe, Germany) with excitation at 550 nm and emission at 600 nm. For EVs remained at the injury site in mice femoral fracture, DID label sEVs were injected for five consecutive days at the fracture site, the mice were imaged with excitation at 640 nm and emission at 700 nm.

2.18. In Vivo evaluation of the osteogenesis of PEEK/PDA/Ti8-21-sEV scaffolds

To evaluate the bone regeneration ability of the PEEK/PDA/Ti8-sEV scaffolds, 20 New Zealand white rabbits (male, 2.5 kg, 6 months old)

were procured from the Institute of Laboratory Animal Science of Huazhong University of Science and Technology (Wuhan, China). All animal studies were approved by the Animal Experimentation Committee of Huazhong University of Science and Technology (Wuhan, China). After anesthesia with Sumianxin (0.15 mL/kg), we used a drill to
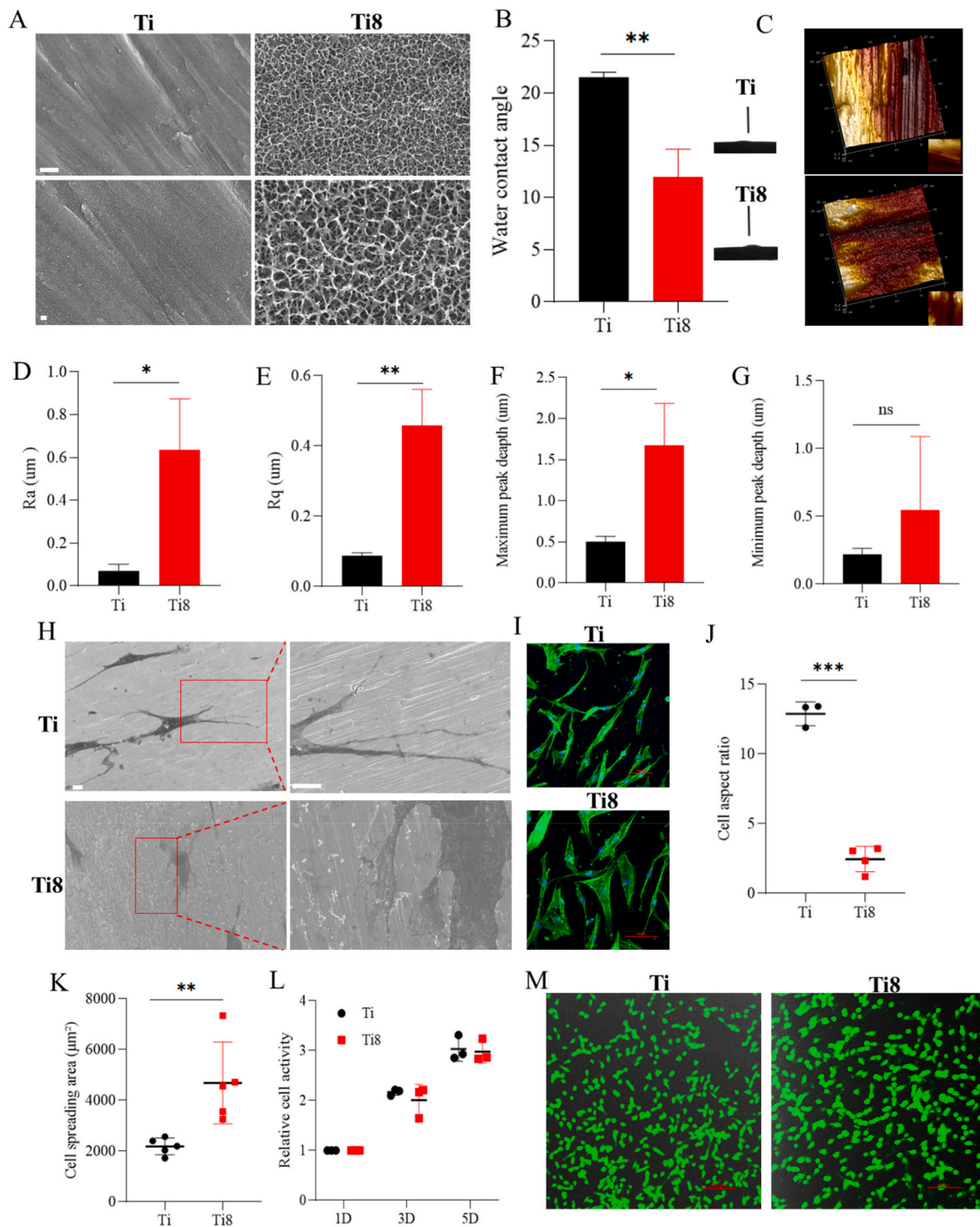
Fig. 2. Characterization of nanotopographic on titanium (Ti) and morphological changes of hMSCs on corresponding surfaces. (A) Surface morphologies characterization of different samples under SEM, Scale bars = 1 μm (first panel) and 200 nm (second panel). (B) Contact angles of different samples. (C) AFM images of the different samples. (D, E, F, G) Ra, Rq, Maximum peak depth and Minimum peak depth of the different Ti samples. (H) SEM of morphologies of hMSCs on different Ti samples, Scale bars = 20 μm (first panel) and 10 μm (second panel). (I) Fluorescent images of cell morphologies on different Ti samples, Scale bars = 100 μm. (J) Quantitative cell spreading area based on SEM images. (K) Quantitative cell aspect ratio based on SEM images. (L) Cell viability based on CCK 8. (M) Live-Dead staining of hMSCs cultured on different Ti samples, Scale bars = 500 μm. Statistical significance: *P < 0.05, **P < 0.01, ***P < 0.001 versus the Ti group, n.s. not significant.

create two femoral condyle defects ($\Phi = 5$ mm, H $= 10$ mm) on each side of the rabbits and the various PEEK scaffolds were implanted. Antibiotics were administered continuously for the first three days after surgery to prevent bacterial infection. The group with the PEEK scaffolds was set as the control group.

2.19. Micro-CT

The bone was scanned using a Micro-CT system (SkyScan 1176, Bruker, Germany). The scanning thickness was 9 μm for mice and 18 μm for rabbits. CT-Vox software was used to reconstruct the 3D images for further analysis. Parameters such as BV/TV, Tb.Th, Tb.N, Tb.Sp, and BMD were analyzed using CTAN software.

2.20. Biomechanical test

Mechanical test for fracture-healing quality were investigated using three-point bending by a testing machine (Electronic Universal Testing Machine, WDW-20, Changchun, China) equipped with a 2000 N load cell. A pushing rod with diameter 2 mm was used to load the sample vertically downward with speed of 1 mm/min.

2.21. Histologic and immunohistochemistry evaluation

Fracture samples of the mice were first decalcified and stained with H&E, Masson's trichrome, and Safranin-O and Fast Green staining. thresholds was used to demonstrate the new bone and to distinguish fibrous tissue, Masson's trichrome staining was used to observe newly formed bone tissue and collagen fiber, Safranin-O/Fast Green staining was used to demonstrate the endochondral ossification. Then, the stained samples were observed and photographed by an optical microscope (Nikon H600L, Tokyo, Japan). In addition, immunohistochemical staining of OCN was applied for the evaluation of new bone. As our previous studies [34], Van Gieson staining was used for the rabbit femoral condyle specimen to evaluate the bone tissue regeneration, and red color denoted as new bone.

2.22. Statistical analysis

Each experiment was repeated at least three times. The data were evaluated as mean ± standard deviation (SD) and were analyzed using GraphPad Instant Software (GraphPad Prism Software, Inc., USA). One-way analysis of variance (ANOVA), two-way ANOVA, and *t*-test were used to evaluate the statistical significance of the variance. *P < 0.05, **P < 0.01, and **P < 0.001 was considered statistically significant.

3. Results and discussion

3.1. Surface physicochemical properties of Ti and cell morphology

Nanomorphology was developed on titanium plates through alkali and heat treatment with 8 M NaOH, and the resulting structure was denoted as Ti8. Firstly, scanning electron microscopy (SEM) was used to observe the morphology of the titanium plates. We can clearly observe that the nanomorphology on Ti8 is similar to the trabecular bone morphology (Fig. 2A). Then, we tested the hydrophilicity of the Ti8 samples. The results showed that the Ti8 sample had better hydrophilicity than Ti, which supported cell adhesion (Fig. 2B). We used atomic force microscopy (AFM) to further characterize the Ti8 morphology (Fig. 2C); the results were consistent with the SEM images. The statistics show that the root-mean-squared (Rq) and absolute (Ra) roughness differed significantly between Ti8 and Ti (Fig. 2D and E). This indicated that the roughness of the titanium plates increased significantly after alkali heat treatment. The maximum and minimum peak depths were also calculated; the results showed that Ti8 had greater maximum peak depth than Ti (P < 0.05), and there was no difference in the minimum

peak depth between Ti8 and Ti (Fig. 2F and G).

The initial adhesion of stem cells on the surface of the biomaterial is important for cell proliferation and differentiation. After culture on Ti and Ti8 for 24 h, we used SEM to observe the morphology of the cells. We can see that after culture on the Ti sample, the cells show an elongated shape with long protruding pseudopods, but in the Ti8 sample, the cells show extensive spreading and have a relatively polygonal shape (Fig. 2H). F-actin fluorescent images of the cell spreading morphology after culturing for 24 h was consistent with the SEM image (Fig. 2I). The quantitative results of the cell spreading area showed that cells growing on Ti8 have better spreading tendency than those growing on Ti (Fig. 2J). The quantitative results of the cell aspect ratio indicated that cells growing on Ti8 spread extensively (Fig. 2K). The results of the cell viability test showed that the cells proliferate gradually with increase in time, and Ti8 has the same effect on cell viability as Ti; this indicated that the Ti8 nanotopography does not promote cell proliferation (Fig. 2L). Live/dead staining further demonstrated that there was no difference in cell activity between Ti8 and Ti (Fig. 2M).

3.2. Enhancement of osteogenesis by nanotopography and sEV characterization

Cells can sense mechanobiological cues such as stiffness and topographical signals [35]. In particular, nanotopographical cues have been incorporated into biomaterials to regulate the cell response. Next, we investigated whether nanotopography can induce hMSC osteogenesis, and studied the characteristics of sEV secreted from hMSC cultured on Ti and Ti8 (Fig. 3A). After culturing hMSCs on Ti and Ti8 for 7, 14 and 21 days, respectively, alkaline phosphatase (ALP) and Alizarin red S (ARS) staining results indicated that nanotopography on Ti8 could significantly promote hMSC differentiation after 21 d (Fig. 3B and Fig. S1A). The quantitative results showed that Ti8 significantly promoted stem cell differentiation when compared with Ti after 21 d, and the difference was statistically significant (Fig. 3C and D). As shown in Figs. S1B and C, there were also statistically significant differences between Ti and Ti8 after 14 d. In order to further verify the osteogenic ability of nanotopography on Ti8, osteogenesis makers including RUNX2, OPN, ALP and OCN were conducted by qRT-PCR. As shown in Figs. S1D, E, F and G, after 21 d, nanotopography on Ti8 significantly promotes osteogenesis of hMSC. Zhuang et al. demonstrated that alkali- and heat-treated Ti with a nanoporous network has better cell proliferation and higher osteogenesis activity [36]. Popat et al. indicated that nanoporous alumina surfaces have superior ability to promote osteogenic differentiation [37]. Cai et al. found that alkali- and heat-treated Ti substrates have great potential for differentiation of MSC [38]. Then, we investigated the effect of nanomorphology on the characteristics of sEV secreted by hMSC. Transmission electron microscopy (TEM) images with higher and lower magnification showed that Ti-21-sEV and Ti8-21-sEV had spherical particles (Fig. 3E and Fig. S2). Surface markers were used to confirm the sizes of sEV through WB and NTA, which further confirmed the presence of sEV (Fig. 3F and G). The sizes of the sEV were approximately 50–150 nm, which was consistent with the results reported in previous studies [39,40]. Subsequently, we investigated whether nanotopography-derived sEV could be internalized by hMSC. We used PKH 26 to label Ti-21-sEV and Ti8-21-sEV, and incubated them with hMSC for 24 h. We can see that most of the sEV were internalized after 24 h, and there was no difference in the number of sEV internalized through cells (Fig. 3H).

3.3. Nanotopography-derived sEV promotes osteogenesis in vitro

sEV have attracted considerable attention for tissue engineering because of their bioactivity [41]. MSC-derived sEV with biocompatibility and immunomodulatory properties have become therapeutic carriers for bone regeneration [42,43]. Using sEVs from surfaces with certain design elements has been studied for several years. Liang et al.
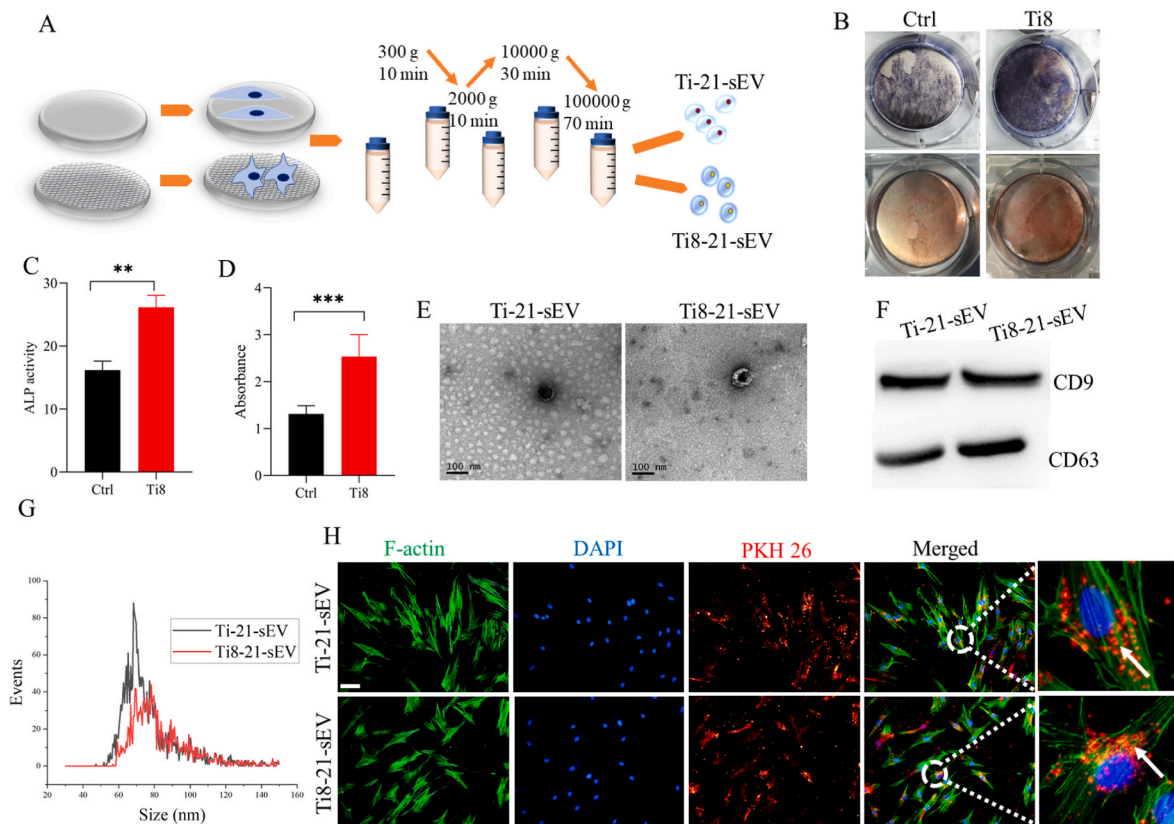
Fig. 3. Nanotopographic promote hMSC differentiation and characterization of sEV. (A) Scheme illustration of nanotopographic promote hMSC differentiation and obtained sEV through different centrifugation. (B) ALP and ARS staining of hMSC cultured on nanotopographic after 21 days. (C, D) Quantitative results of ALP and ARS staining of hMSC cultured on nanotopographic after 21 days. (E) TEM image of Ti-21-sEV and Ti8-21-sEV, Scale bars = 100 nm. (F) Expression of CD9 and CD63 protein was assessed by a Western blot assay. (G) Nanoparticle tracking analysis (NTA) of sEV. (H) Internalization of PKH26-labeled sEV by hMSC, Scale bars = 200 μm **p < 0.01, ***p < 0.001.

found that endothelial cells morphology can affect the function of themselves and then regulated the inflammatory response of monocytes. They demonstrated that endothelial cells with elongated morphology cultured on microgrooves surface can significantly suppressed the activity of the monocytes in comparison with a cobblestone shape [44]. Francesco et al. analyzed a porous scaffold to promote the astrocytes to grow, survive and differentiate. They revealed that astrocytes adhere, grow well on the scaffolds and the extracellular vesicles secreted from astrocytes were compatible in size with exosomes [45]. Wan et al. developed a one-step nEV isolation platform which included a nano-structures with sEV size-matched silica and a surface-conjugated lipid nanoprobe, and this platform can improve the cancer diagnosis [46]. Liu et al. showed that Micro/nano materials regulate endothelial cells morphology and transferred sEV to smooth muscle cells and regulate their phenotype [47]. However, the ability of topographic signals to regulate the sEV function of hMSC has not yet been reported. In this study, we collected Ti-21-sEV and Ti8-21-sEV, and investigated whether nanotopography-trained stem cells could secrete sEV with pro-osteogenic potential (Fig. 4A). ALP and ARS staining showed that compared with the control, Ti-21-sEV and Ti8-21-sEV have superior pro-differentiation ability, and Ti8-21-sEV has better ability to promote osteogenesis (Fig. 4B). To further verify the pro-osteogenic ability of Ti8-21-sEV, we then used immunofluorescence (IF) to further investigate the pro-osteogenic ability of Ti8-21-sEV. The result was consistent with the results of ALP and ARS staining. Osteogenesis related markers including RUNX2, OCN and ALP showed that Ti8-21-sEV had remarkable ability to induce differentiation of hMSC (Fig. 4C). As our previous study [3], we selected early osteogenesis related marker OPN, a master determinant of osteoblast differentiation of transcription factor RUNX2

[48] and osteoblast marker genes ALP [49] to further verify the pro-osteogenic ability of Ti8-21-sEV through qRT-PCR. After incubation with Ti8-21-sEV for 7 days, the expression of OPN, RUNX2, and ALP was significantly higher than that in the control group (Fig. 4D, E, F). In summary, our data suggested that nanotopography could train stem cells to secrete sEV with pro-osteogenic potential.

3.4. Nanotopography-derived sEV promotes osteogenesis in vivo

In order to validate the osteogenesis ability of sEV. We used a mouse fracture model to verify the pro-osteogenic effect of Ti8-21-sEV by injecting them at the fracture site for 5 consecutive days (Fig. 5A). EVs remained at the injury site were explored using imaging system, as shown in Fig. S3, after five consecutive days of injection, we can see that many DID label sEVs accumulated at the fracture site, and when we stopped injection after 24 h (6 D) and 48 h (7D), DID labeled sEVs began to decrease. Therefore, we found that five consecutive days of injection ensured that the vesicles accumulated well at the fracture site and remained there for at least 48 h. Micro CT observations showed that after 14 days, Ti8-21-sEV significantly promoted new bone formation when compared with the control group. After 21 days, new bone remodeling was evident and cortical bone was formed gradually when compared with the control group (Fig. 5B). Mechanical test for detecting the fracture-healing quality were performing through three-point bending biomechanical test, the result indicated that compared with control group, injection of Ti8-21-sEV obviously improved fracture healing at either 14 or 21 days (Fig. 5C). Quantitative analysis of tissue volume (TV) indicated that 14 days after fracture, the formation of new callus gradually decreased and new bone was formed after treatment
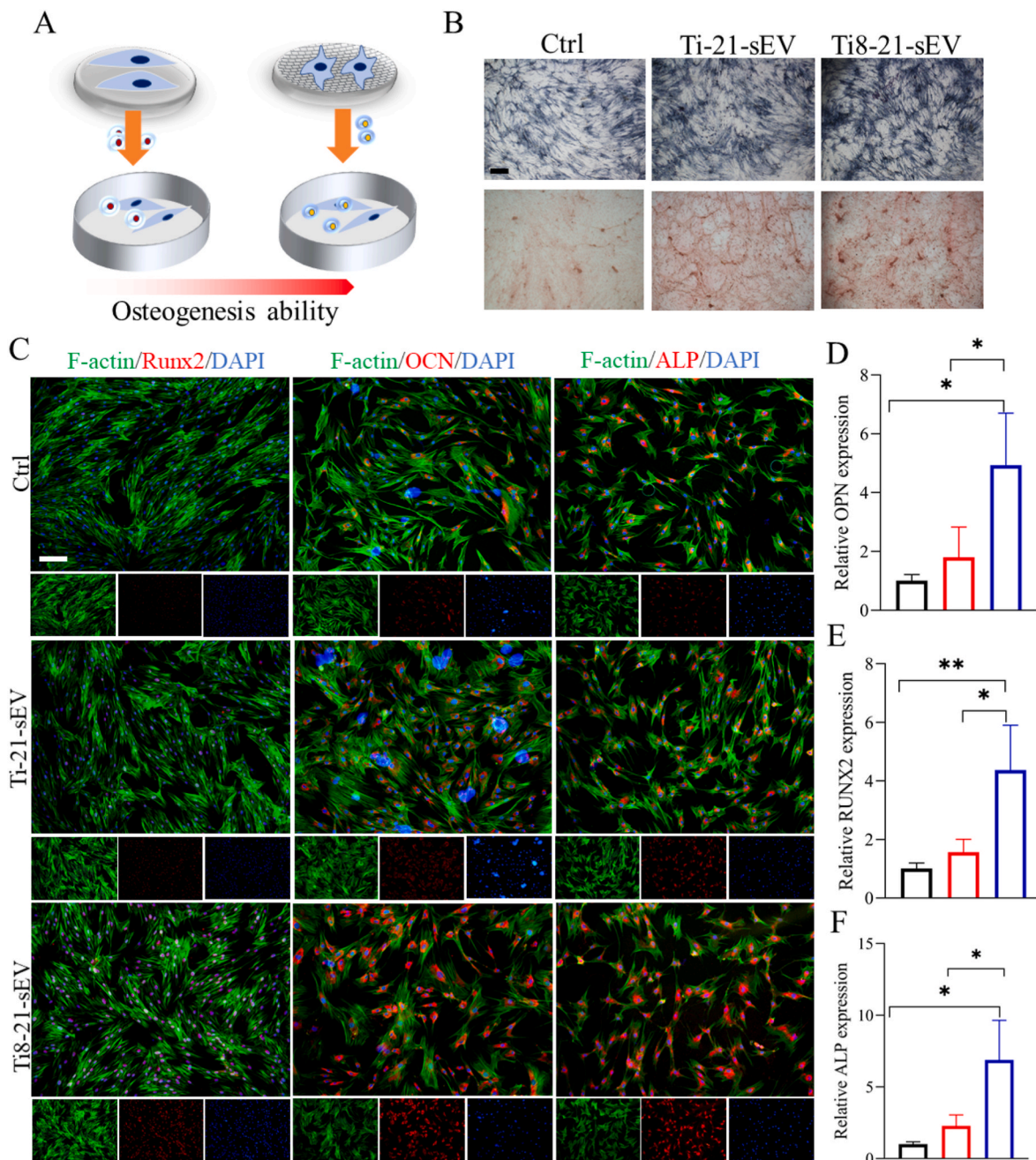
Fig. 4. Pro-osteogenesis ability of Ti8-21-sEV *in vitro*. (A) Scheme illustration of sEV secreted from hMSC cultured on Ti nanotopographic after 21 days (Ti8-21-sEV) and Ti8-21-sEV promote osteogenesis. (B) ALP and ARS staining of hMSC after inculbated with Ti8-21-sEV and Ti-21-sEV for 7 days, Scale bars = 200 μm. (C) Immunofluorescence staining (IF) of osteogenic makers including RUNX2, OCN and ALP of hMSC after inculbated with Ti8-21-sEV and Ti-21-sEV, Scale bars = 200 μm. (D, E, F) Osteogenesis-related makers OPN, RUNX2 and ALP were detected through qRT-PCR. *p < 0.05, **p < 0.01.

with Ti8-21-sEV. After 21 days, there were no significant differences among the groups (Fig. 5D). Bone volume (BV)/TV results showed that Ti8-21-sEV has superior ability to promote new bone after 14 and 21 days (Fig. 5E). The results of trabecular thickness (Tb.Th) and trabecular separation (Tb.Sp) indicated that after 14 and 21 days, there was no significant difference among the three groups (Fig. 5F and G), possible explanation is that the fracture period we studied was three weeks, which may too short to show significant changes on Tb. Th and Tb. Sp in the early stages of osteogenesis. Dou et al. demonstrated that cerium nano-system attenuated bone loss in osteoporotic OVX mice through selectively eliminated mature osteoclasts without affecting pre-osteoclasts [50]. The model we used in our study is a fracture model, which may require a longer observation time, therefore, we will

continue to try to use the osteoporotic OVX mice to verify this in the future. To further strengthen the evidence of pro-osteogenic ability of Ti8-21-sEV, we measured the regeneration of fractured site using same mouse model and the same fracture site after 14 and 21 days through Micro CT. Laperre et al. conducted two micro-CT protocols for offering the unique information of bone mass and structure changes in living mice over time, and they demonstrated that bone structure in living mice can be monitor using micro-CT over 4 weeks without significant side effects when exposure by X-ray [51]. Consistent with measurement results of killed mouses over time using micro-CT in Fig. 5B, Ti8-21-sEV have excellent pro-osteogenic ability after 21 days compared with control group (Fig. S4). Meanwhile, histological staining results of mice femur also showed significant formation of new bone 14 and 21 days
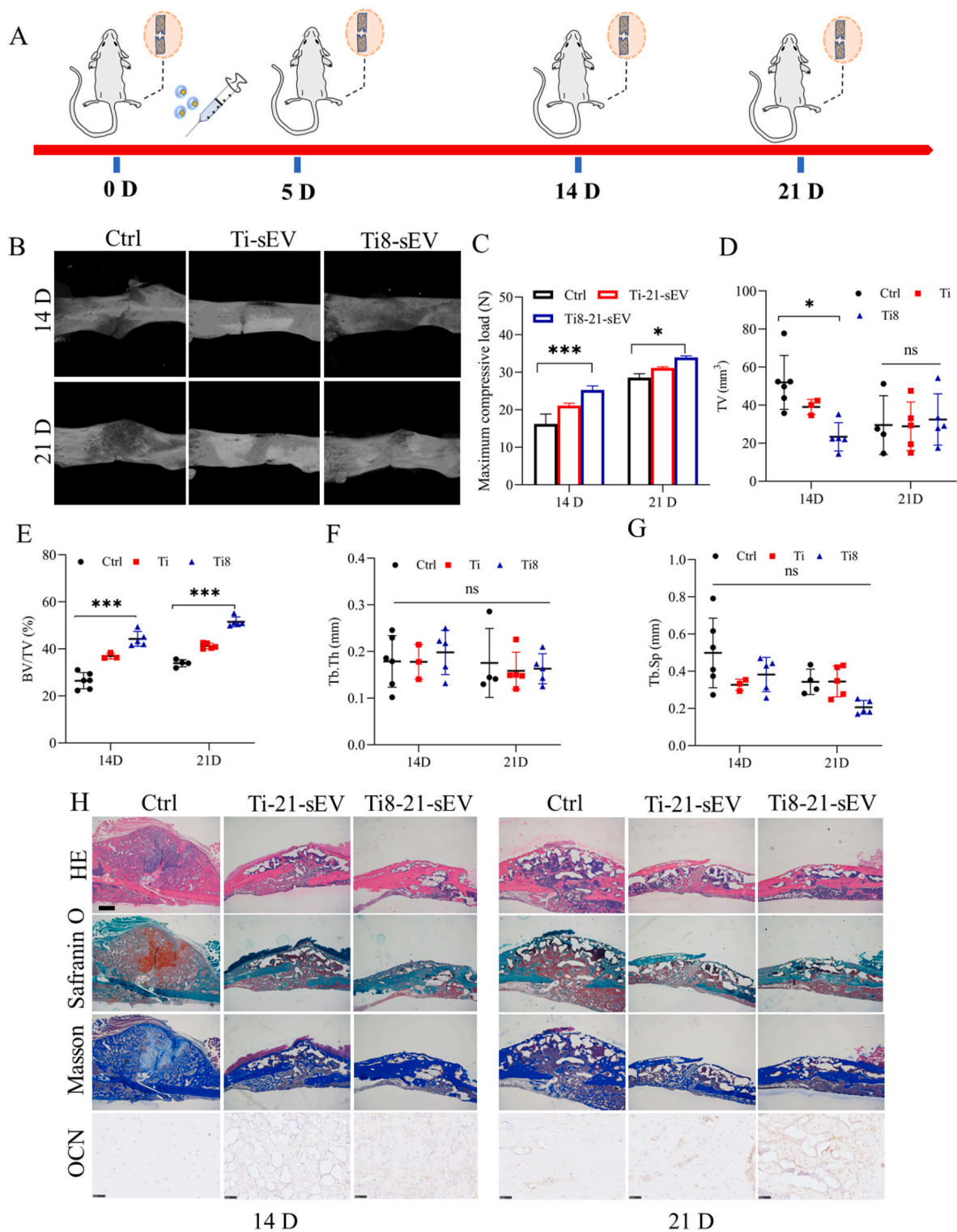
Fig. 5. Pro-osteogenesis ability of Ti8-21-sEV *in vivo*. (A) Scheme illustration of mouse fracture treatment through Ti-21-sEV and Ti8-21-sEV. N = 6 for each group. (B) Micro-CT images of mouse fracture treated by Ti-21-sEV and Ti8-21-sEV after 14 and 21 days. (C) Three-point bending test for measuring the biomechanical strength of the healing bone after 14 and 21 days. *P < 0.05, ***P < 0.001. ns, not significant. (D, E, F, G) TV, BV/TV, Tb. Th and Tb. Sp of the new bone tissue were quantitated based on Micro-CT. (H) Histological staining and immunohistochemical staining of OCN of new bone tissue after 14 and 21 days, Scale bars = 200 μm and 50 μm, respectively.

after treatment with Ti8-21-sEV (Fig. 5H).

3.5. Osteogenesis mechanism of Ti8-21-sEV

To understand how nanotopography-derived sEV promotes osteogenesis, transcriptomic RNA analysis of hMSC incubated with cell medium (A), Ti-21-sEV (B), or Ti8-21-sEV (C) was conducted with A as control (Fig. S5A). Correlation analysis based on Pearson correlation showed that samples from the same group had good consistency (Fig. S5B). The Venn diagram showed differences in gene expressions

and the samples shared 123 genes (Fig. S5C). Heat map analysis and volcano plot data showed that when compared with the hMSCs incubated with cell medium, 1566 genes were up-regulated and 1328 genes were down-regulated in the Ti-21-sEV group, and 1635 genes were up-regulated and 1517 genes were down-regulated in the Ti8-21-sEV group. In comparison with the Ti-21-sEV group, 111 genes were up-regulated and 236 genes were down-regulated in the Ti8-21-sEV group (Figs. S5D and E). These results demonstrate a wide range of different gene expressions. Next, the thresholds of fold change >|2| and p value < 0.05 were used to show differentially expressed genes, and such genes were used to perform gene ontology (GO) analysis of the biological process, cellular components, and molecular function. In comparison with the control, the genes in the Ti-21-sEV group exhibited better developmental process, anatomical structure development, extracellular region, vesicle, carbohydrate derivative binding, and cytoskeletal protein binding (Fig. S6). In comparison with the control group, the differently expressed genes in the Ti8-21-sEV group exhibited better developmental process, anatomical structure development, extracellular region, cytoskeleton, carbohydrate derivative binding, and cytoskeletal protein binding (Fig. S7). To further demonstrate the nanotopographic regulation of hMSC, we compared the cells treated with Ti8-21-sEV or Ti-21-sEV. In comparison with the Ti-21-sEV group, Ti8-21-sEV treatment could induce the participation of different genes in anatomical structure development, positive regulation of cellular process, and cell differentiation (Fig. S8). These cues indicate that Ti8-21-sEV might have superior pro-differentiation ability. To further focus on the effect of vesicles on cell differentiation, we screened for GO term associated with cell differentiation and we displayed the top 10 GO terms associated with cell differentiation using bubble plot. The results showed that in comparison with the control, Ti-21-sEV treatment could regulate Osteoblast differentiation, regulation of cell differentiation, positive regulation of osteoblast differentiation, regulation of osteoblast

differentiation (Fig. 6A). Kyoto Encyclopedia of Genes and Genomes (KEGG) pathway analysis further indicated that multiple pathways are associated with osteogenesis, including the Ras, PI3K-AKT, and p53 signaling pathways, mineral absorption, FoxO signaling pathway, focal adhesion, ECM-receptor interaction, and cell cycle (Fig. 6B). We then compared the Ti8-21-sEV-treated hMSC with the control. The result suggested that Osteoblast differentiation, positive regulation of osteoblast differentiation, positive regulation of cell differentiation, regulation of stem cell differentiation, regulation of cell differentiation might play a major role in promoting osteogenesis (Fig. 6C). The KEGG pathway analysis indicated that Ti8-21-sEV may be involved in regulation of the Ras, PI3K-AKT, and p53 signaling pathways, mineral absorption, MAPK signaling pathway, focal adhesion, ECM-receptor interaction, and cell cycle (Fig. 6D). Finally, we compared Ti-21-sEV with Ti8-21-sEV treated hMSC. The GO term showed that Ti8-21-sEV treatment could induce positive regulation of cell differentiation and cell differentiation (Fig. S9A). KEGG analysis indicated that cytokine–cytokine receptor interaction might be involved in bone regeneration (Fig. S9B). Potential molecular signaling pathways by sEV which secreted from hMSC cultured on nanotopography on Ti surface influence osteogenic differentiation were also depicted (Fig. 6E).

Xu et al. investigated the effects of hydroxyapatite with a different hierarchical structure on the biological responses, and the RNA-seq result indicated that the hierarchical structure of the hydroxyapatite particles could stimulate the osteogenic differentiation of stem cells. In addition, the increased calcium ion endocytosis through lysosomes activated possible Ras/cAMP/Rap1/MAPK signaling pathways, which are involved in osteogenic differentiation [52]. Feng et al. suggested that HMGB1 can induce the secretion of various cytokines by stem cells and promotes osteogenic differentiation through activation of the Ras/-MAPK signaling pathway [53]. Liu et al. showed that immune regulation through 3D-printed electrospun fibrous scaffolds could regulate M2

Fig. 6. Mechanistic analysis of Ti8-21-sEV promote osteogenesis. (A, C) GO term associated with cell differentiation and we displayed the top 10 GO terms associated with cell differentiation using bubble plot. (B, D) Top 20 KEGG pathways of differentially expressed genes. (E) Potential molecular signaling pathways by sEV which secreted from hMSC cultured on nanotopography on Ti surface influence osteogenic differentiation.

macrophage polarization through PI3K/AKT signaling, causing them to secrete VEGF and BMP-2 for enhanced osteogenesis [54]. Dou et al. found that the cerium nanosystem can promote osteogenesis of stem cells and angiogenesis of endothelial progenitor cells through PI3K-Akt activated focal adhesion kinase [50]. Li et al. showed that the ALKBH5-PRMT6 axis could modulate the osteogenic differentiation of stem cells via the PI3K-Akt signaling pathway [55]. Iyer et al. suggested that FOXOs could attenuate Wnt signaling to decrease the number of osteoblasts and amount of bone mass, thereby causing osteoporosis [56]. Vermeulen et al. indicated that natural surfaces improved the TopoChip design space and ensured consistency with the distinct morphological and focal adhesion profiles of mesenchymal stem cells. They demonstrated that holy lotus has strong potential for bone regeneration of stem cells [57]. Ye et al. demonstrated that Mg could enhance the repair of critical-size bone defect through the CGRP-FAK-VEGF signaling axis [58]. In summary, RNA sequencing results indicated
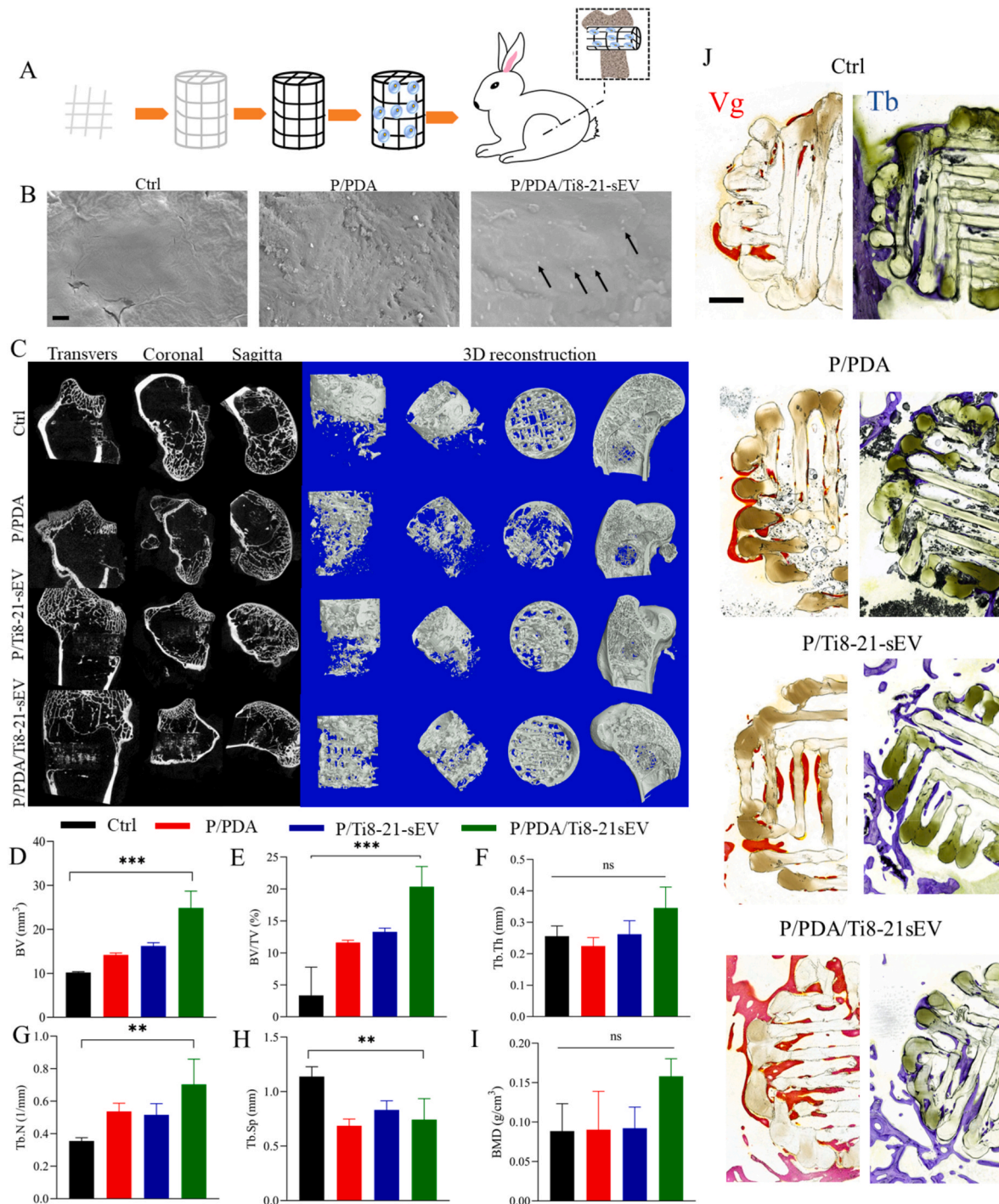
Fig. 7. 3D printed PEEK scaffolds loaded with sEV for bone regeneration. (A) Scheme illustration of implantation of 3D printed PEEK scaffolds loaded with sEV into femoral condyle defect of rabbit. (B) SEM images of PEEK plates, PEEK/PDA plates and PEEK/PDA/Ti8-21-sEV plates. Black arrow: Ti8-21-sEV, Scale bars = 1 μm. (C) 2D (transverse, coronal, and sagittal) and 3D reconstruction images based on Micro CT after 12 weeks. (D, E, F, G, H, I) Quantitative results of BV, BV/TV, Tb. Th, Tb. N, Tb. Sp and BMD among the different groups. (J) Van-Gieson (VG) and Toluidine blue staining of histological sections after implanted for 12 weeks. **p < 0.01, ***p < 0.001, ns, not significant.

that nanotopography triggered the stem cells to secrete sEV to promote osteogenesis *via* the Ras signaling pathway, PI3K-AKT signaling pathway, p53 signaling pathway, MAPK signaling pathway, mineral absorption, FoxO signaling pathway, focal adhesion, ECM-receptor interaction, and cell cycle.

3.6. Tissue engineering application of nanotopography-derived sEV

In order to exploit the sEV for bone tissue engineering, we used a 3D printed PEEK scaffold to load the Ti8-21-sEV to investigate bone regeneration using the classic rabbit femoral condyle defect model (Fig. 7A). First, the morphological characteristics of different PEEK scaffolds were observed through SEM. We can see that the scaffolds have a porous structure (Fig. S10A). Then, the morphology of the stem cells on different PEEK scaffolds after culturing for 24 h were observed using SEM. The cells showed satisfactory growth on the scaffolds, and the polydopamine (pDA) coating benefited the adhesion and stretching of the stem cells (Fig. S10B). Next, we used circular PEEK plates to observe the loaded vesicles. After pDA coating, we could observe the dopamine aggregated in the particles. We further observed that the sEV were distinct from the dopamine particles and were dispersed on the PEEK plates (Fig. 7B). DID labeled sEV also confirmed that sEV evenly distributed on PEEK plates surface through the observation of confocal laser scanning microscope (Fig. S10C). Next, we investigated the absorption of Ti8-21-sEV *in vivo*. We concluded that Ti8-21-sEV is slowly released and absorbed after 7 days (Fig. S10D). We continued to investigate the ability of Ti8-21-sEV decorated on PEEK/pDA scaffolds *in vivo* using the classic rabbit femoral condyle defect model. After implantation of different PEEK scaffolds for 6 and 12 weeks, new bone regeneration was evaluated through micro-CT and histological analysis. After 6 weeks, the reconstructed micro-CT images revealed that new bone regeneration was significantly greater in the PEEK/PDA/Ti8-21-sEV group than that in the other groups (Fig. S11A). Quantitative BV results and the BV/TV ratio showed that after decoration with Ti8-21-sEV, the osteogenic ability of the PEEK scaffolds was significantly enhanced, and a greater amount of new bone tissue was generated (Figs. S11B and C). The quantitative results showed significant increase in the Tb. Th (Fig. S11D). There was no significant difference in the number and separation of the trabecular bone (Tb. N and Tb. Sp) and bone mineral density (BMD) among the groups after 6 weeks (Figs. S10E, F, G). Van Gieson (VG) and Toluidine blue staining further revealed the new bone tissue regeneration, and several new bones were observed in the PEEK/pDA/Ti8-21-sEV group 6 weeks after scaffold implantation (Fig. S11H). After 12 weeks, there was significant new bone formation in the PEEK/PDA/Ti8-21-sEV group based on micro-CT observation (Fig. 7C). Quantitative results of BV and BV/TV indicated that the PEEK/pDA/Ti8-21-sEV group had significant pro-osteogenesis ability and showed statistically significant differences from the control group (Fig. 7D and E). There was no significant difference in Tb.Th among the groups, which suggested that new bone remodeling was complete after 12 weeks (Fig. 7F). Quantitative results of the trabecular number (Tb.N) and Tb.Sp further demonstrated that in comparison with the control group, Ti8-21-sEV could significantly increase the number of trabecular bones and decrease the degree of separation of the trabecular bone (Fig. 7G and H). Quantitative results of BMD showed that there was no significant difference among the four groups (Fig. 7I). The VG and Toluidine blue staining assays further indicated that the PEEK scaffolds decorated with Ti8-21-sEV could significantly induce new bone formation owing to a large number of new bones growing along the scaffold (Fig. 7J). Overall, the above findings suggest that Ti8-21-sEV can be used for bone tissue engineering to induce bone regeneration.

In summary, compared with traditional titanium (Ti) metals, PEEK is considered a potential substitute for traditional Ti implants owing to appropriate elastic modulus, natural radiolucency, and chemical resistance. However, the poor bioactivity impedes bone ingrowth after implantation [59–61]. In this study, we used the 3D printing technology to manufacture PEEK scaffolds with a porous structure. Further, polydopamine not only acts as an intermediate for sEV immobilization but also provides a powerful route for enhancing cell adhesion [2,62].

4. Conclusion

In this work, we successfully performed nanotopography on Ti plates through alkali and heat treatment, and demonstrated that Ti8-21-sEV have memory function by copying the pro-osteogenesis information from nanotopography. It was also revealed that Ti8-21-sEV-loaded 3D printing PEEK scaffolds have better bone ingrowth ability than the other scaffolds based on the application of the scaffolds to the femoral condyle defect model of rabbit. However, there are still some limitations. First, osteogenesis related signaling pathways have been predicted by RNA sequencing, in the following study in the future, we will verify these possible osteogenic signaling pathways in cellular and animal level, and we will continue to explore whether other nanomorphologies have similar pro-osteogenesis functions and possible altered signaling pathways. Second, the more important question is regarding the cargo of the EVs which carrying miRNAs, proteins, lipids and DNA, continued to explore what kind of cargo of the vesicles are changed by the nanotopography are important in the following study. We believe our study can inspire the design of other sEV with morphology memory function for tissue regeneration.

CRediT authorship contribution statement

Liang Ma: Investigation, Data curation, Formal analysis, Writing – original draft. **Wencan Ke:** Investigation, Data curation, Visualization. **Zhiwei Liao:** Investigation, Methodology. **Xiaobo Feng:** Investigation, Methodology. **Jie Lei:** Methodology. **Kun Wang:** Methodology. **Bingjin Wang:** Methodology. **Gaocai Li:** Methodology. **Rongjin Luo:** Methodology. **Yunsong Shi:** Methodology. **Weifeng Zhang:** Resources. **Yu Song:** Supervision. **Weibin Sheng:** Resources. **Cao Yang:** Conceptualization, Supervision, Writing – review & editing, Formal analysis.

Acknowledgements

Appendix A. Supplementary data

Supplementary data to this article can be found online at https://doi.org/10.1016/j.bioactmat.2022.01.008.

References

[1] X. Zhang, M. Xu, L. Song, Y. Wei, Y. Lin, W. Liu, B.C. Heng, H. Peng, Y. Wang, X. Deng, Effects of compatibility of deproteinized antler cancellous bone with various bioactive factors on their osteogenic potential, Biomaterials 34 (2013) 9103–9114, https://doi.org/10.1016/j.biomaterials.2013.08.024.

[2] W. Li, Y. Liu, P. Zhang, Y. Tang, M. Zhou, W. Jiang, X. Zhang, G. Wu, Y. Zhou, Tissue-engineered bone immobilized with human adipose stem cells-derived exosomes promotes bone regeneration, ACS Appl. Mater. Interfaces 10 (2018) 5240–5254, https://doi.org/10.1021/acsami.7b17620.

[3] L. Ma, X. Feng, H. Liang, K. Wang, Y. Song, L. Tan, B. Wang, R. Luo, Z. Liao, G. Li, X. Liu, S. Wu, C. Yang, A novel photothermally controlled multifunctional scaffold for clinical treatment of osteosarcoma and tissue regeneration, Mater. Today 36 (2020) 48–62, https://doi.org/10.1016/j.mattod.2019.12.005.

[4] T. Zhang, Q. Wei, H. Zhou, Z. Jing, X. Liu, Y. Zheng, H. Cai, F. Wei, L. Jiang, M. Yu, Y. Cheng, D. Fan, W. Zhou, X. Lin, H. Leng, J. Li, X. Li, C. Wang, Y. Tian, Z. Liu, Three-dimensional-printed individualized porous implants: a new "implant-bone" interface fusion concept for large bone defect treatment, Bioact. Mater. 6 (2021) 3659–3670, https://doi.org/10.1016/j.bioactmat.2021.03.030.

[5] V. Fitzpatrick, Z. Martin-Moldes, A. Deck, R. Torres-Sanchez, A. Valat, D. Cairns, C. Li, D.L. Kaplan, Functionalized 3D-printed silk-hydroxyapatite scaffolds for enhanced bone regeneration with innervation and vascularization, Biomaterials 276 (2021) 120995, https://doi.org/10.1016/j.biomaterials.2021.120995.

[6] M. Mehta, K. Schmidt-Bleek, G.N. Duda, D.J. Mooney, Biomaterial delivery of morphogens to mimic the natural healing cascade in bone, Adv. Drug Deliv. Rev. 64 (2012) 1257–1276, https://doi.org/10.1016/j.addr.2012.05.006.

[7] M. Zhai, Y. Zhu, M. Yang, C. Mao, Human mesenchymal stem cell derived exosomes enhance cell-free bone regeneration by altering their miRNAs profiles, Adv. Sci. 7 (2020) 2001334, https://doi.org/10.1002/advs.202001334.

[8] M. Lian, B. Sun, Y. Han, B. Yu, W. Xin, R. Xu, B. Ni, W. Jiang, Y. Hao, X. Zhang, Y. Shen, Z. Qiao, K. Dai, A low-temperature-printed hierarchical porous sponge-like scaffold that promotes cell-material interaction and modulates paracrine activity of MSCs for vascularized bone regeneration, Biomaterials 274 (2021) 120841, https://doi.org/10.1016/j.biomaterials.2021.120841.

[9] M. Maruyama, A. Nabeshima, C.C. Pan, A.W. Behn, T. Thio, T. Lin, J. Pajarinen, T. Kawai, M. Takagi, S.B. Goodman, Y.P. Yang, The effects of a functionally-graded scaffold and bone marrow-derived mononuclear cells on steroid-induced femoral head osteonecrosis, Biomaterials 187 (2018) 39–46, https://doi.org/10.1016/j.biomaterials.2018.09.030.

[10] F. Manzoor, A. Golbang, S. Jindal, D. Dixon, A. McIlhagger, E. Harkin-Jones, D. Crawford, E. Mancuso, 3D printed PEEK/HA composites for bone tissue engineering applications: effect of material formulation on mechanical performance and bioactive potential, J. Mech. Behav. Biomed. Mater. 121 (2021) 104601, https://doi.org/10.1016/j.jmbbm.2021.104601.

[11] D. Xie, C. Xu, C. Ye, S. Mei, L. Wang, Q. Zhu, Q. Chen, Q. Zhao, Z. Xu, J. Wei, L. Yang, Fabrication of submicro-nano structures on polyetheretherketone surface by femtosecond laser for exciting cellular responses of MC3T3-E1 cells/gingival epithelial cells, Int. J. Nanomed. 16 (2021) 3201–3216, https://doi.org/10.2147/IJN.S303411.

[12] R. Ma, T. Tang, Current strategies to improve the bioactivity of PEEK, Int. J. Mol. Sci. 15 (2014) 5426–5445, https://doi.org/10.3390/ijms15045426.

[13] W.T. Lee, J.Y. Koak, Y.J. Lim, S.K. Kim, H.B. Kwon, M.J. Kim, Stress shielding and fatigue limits of poly-ether-ether-ketone dental implants, J. Biomed. Mater. Res. B Appl. Biomater. 100 (2012) 1044–1052, https://doi.org/10.1002/jbm.b.32669.

[14] I. Nakahara, M. Takao, S. Bandoh, N. Bertollo, W.R. Walsh, N. Sugano, In vivo implant fixation of carbon fiber-reinforced PEEK hip prostheses in an ovine model, J. Orthop. Res. 31 (2013) 485–492, https://doi.org/10.1002/jor.22251.

[15] C. Zhu, M. He, L. Mao, T. Li, L. Zhang, L. Liu, G. Feng, Y. Song, Titanium-interlayer mediated hydroxyapatite coating on polyetheretherketone: a prospective study in patients with single-level cervical degenerative disc disease, J. Transl. Med. 19 (2021) 14, https://doi.org/10.1186/s12967-020-02688-z.

[16] M. Al-Rabab'ah, W. Hamadneh, I. Alsalem, A. Khraisat, A. Abu Karaky, Use of high performance polymers as dental implant abutments and frameworks: a case series report, J. Prosthodont. 28 (2019) 365–372, https://doi.org/10.1111/jopr.12639.

[17] Y. Ji, H. Zhang, J. Ru, F. Wang, M. Xu, Q. Zhou, H. Stanikzai, I. Yerlan, Z. Xu, Y. Niu, J. Wei, Creating micro-submicro structure and grafting hydroxyl group on PEEK by femtosecond laser and hydroxylation to synergistically activate cellular response, Mater. Des. 199 (2021), https://doi.org/10.1016/j.matdes.2020.109413.

[18] M. Zhao, M. An, Q. Wang, X. Liu, W. Lai, X. Zhao, S. Wei, J. Ji, Quantitative proteomic analysis of human osteoblast-like MG-63 cells in response to bioinert implant material titanium and polyetheretherketone, J. Proteonomics 75 (2012) 3560–3573, https://doi.org/10.1016/j.jprot.2012.03.033.

[19] F.B. Torstrick, A.S.P. Lin, D. Potter, D.L. Safranski, T.A. Sulchek, K. Gall, R. E. Guldberg, Porous PEEK improves the bone-implant interface compared to plasma-sprayed titanium coating on PEEK, Biomaterials 185 (2018) 106–116, https://doi.org/10.1016/j.biomaterials.2018.09.009.

[20] M. He, C. Zhu, H. Xu, D. Sun, C. Chen, G. Feng, L. Liu, Y. Li, L. Zhang, Conducting polyetheretherketone nanocomposites with an electrophoretically deposited bioactive coating for bone tissue regeneration and multimodal therapeutic applications, ACS Appl. Mater. Interfaces 12 (2020) 56924–56934, https://doi.org/10.1021/acsami.0c20145.

[21] J. Yan, D. Xia, W. Zhou, Y. Li, P. Xiong, Q. Li, P. Wang, M. Li, Y. Zheng, Y. Cheng, pH-responsive silk fibroin-based CuO/Ag micro/nano coating endows polyetheretherketone with synergistic antibacterial ability, osteogenesis, and angiogenesis, Acta Biomater. 115 (2020) 220–234, https://doi.org/10.1016/j.actbio.2020.07.062.

[22] C. Thery, K.W. Witwer, E. Aikawa, M.J. Alcaraz, J.D. Anderson, R. Andriantsitohaina, A. Antoniou, T. Arab, F. Archer, G.K. Atkin-Smith, D.C. Ayre, J.M. Bach, D. Bachurski, H. Baharvand, L. Balaj, S. Baldacchino, N.N. Bauer, A. A. Baxter, M. Bebawy, C. Beckham, A. Bedina Zavec, A. Benmoussa, A.C. Berardi, P. Bergese, C. Bielska, S. Blenkiron, E. Bobis-Wozowicz, W. Boilard, A. Boireau, F. E. Bongiovanni, S. Borras, C.M. Bosch, S. Boulanger, A.M. Breakefield, M. A. Breglio, D.R. Brennan, A. Brigstock, M.L. Brisson, J.F. Broekman, P. Bromberg, S. Bryl-Gorecka, A.H. Buch, D. Buck, S. Burger, D. Busatto, B. Buschmann, E. I. Bussolati, J.B. Buzas, G. Byrd, D.R. Camussi, S. Carter, L.W. Caruso, Y. T. Chamley, C. Chang, S. Chen, L. Chen, A.R. Cheng, A. Chin, S.P. Clayton, A. Clerici, E. Cocks, R.J. Cocucci, A. Coffey, Y. Cordeiro-da-Silva, F.A. Couch, B. Coumans, R. Coyle, M.F. Crescitelli, Criado, C. D'Souza-Schorey, S. Das, A. Datta Chaudhuri, P. de Candia, E.F. De Santana, O. De Wever, H.A. Del Portillo, T. Demaret, S. Deville, A. Devitt, B. Dhondt, D. Di Vizio, L.C. Dieterich, V. Dolo, A. P. Dominguez Rubio, M. Dominici, M.R. Dourado, T.A. Driedonks, F.V. Duarte, H. M. Duncan, R.M. Eichenberger, K. Ekstrom, S. El Andaloussi, C. Elie-Caille, U. Erdbrugger, J.M. Falcon-Perez, F. Fatima, J.E. Fish, M. Flores-Bellver, A. Forsonits, A. Frelet-Barrand, F. Fricke, G. Fuhrmann, S. Gabrielsson, A. Gamez-Valero, C. Gardiner, K. Gartner, R. Gaudin, Y.S. Gho, B. Giebel, C. Gilbert,

M. Gimona, I. Giusti, D.C. Goberdhan, A. Gorgens, S.M. Gorski, D.W. Greening, J. C. Gross, A. Gualerzi, D. Gupta, A. Gustafson, R.A. Handberg, P. Haraszti, H. Harrison, A. Hegyesi, A.F. Hendrix, F.H. Hill, K.F. Hochberg, B. Hoffmann, H. Holder, B. Holthofer, G. Hosseinkhani, Y. Hu, Huang, V. Huber, S. Hunt, A. G. Ibrahim, T. Ikezu, J.M. Inal, M. Isin, A. Ivanova, H.K. Jackson, S. Jacobsen, S. M. Jay, M. Jayachandran, G. Jenster, L. Jiang, S.M. Johnson, J.C. Jones, A. Jong, T. Jovanovic-Talisman, S. Jung, R. Kalluri, S.I. Kano, S. Kaur, Y. Kawamura, E. T. Keller, D. Khamari, E. Khomyakova, A. Khvorova, P. Kierulf, K.P. Kim, T. Kislinger, M. Klingeborn, D.J. Klinke, M. Kornek 2nd, M.M. Kosanovic, A. F. Kovacs, E.M. Kramer-Albers, S. Krasemann, M. Krause, I.V. Kurochkin, G. D. Kusuma, S. Kuypers, S. Laitinen, S.M. Langevin, L.R. Languino, J. Lannigan, C. Lasser, L.C. Laurent, G. Lavieu, E. Lazaro-Ibanez, S. Le, M.S. Lay, Y.X.F. Lee, D. S. Lee, M. Lemos, A. Lenassi, I.T. Leszczynska, K. Li, S.F. Liao, E. Libregts, R. Ligeti, S.K. Lim, A. Lim, K. Line, A. Linnemannstons, C.A. Llorente, M.J. Lombard, A. M. Lorenowicz, J. Lorincz, J. Lotvall, M.C. Lovett, X. Lowry, Q. Loyer, B. Lu, T. R. Lukomska, S.L. Lunavat, H. Maas, A. Malhi, J. Marcilla, J. Mariani, E.S. Mariscal, L. Martens-Uzunova, M.C. Martin-Jaular, V.R. Martinez, M. Martins, S. Mathieu, M. Mathivanan, L.K. Maugeri, M.J. McGinnis, D.G. McVey, Meckes Jr., K. L. Meehan, I. Mertens, V.R. Minciacchi, A. Moller, M. Moller Jorgensen, A. Morales-Kastresana, J. Morhayim, F. Mullier, L. Muraca, V. Musante, D. C. Mussack, K.H. Muth, T. Myburgh, M. Najrana, I. Nawaz, P. Nazarenko, C. Nejsum, T. Neri, R. Neri, L. Nieuwland, J.P. Nimrichter, E.N. Nolan, Nolte-'t Hoen, N. Noren Hooten, L. O'Driscoll, T. O'Grady, A. O'Loghlen, T. Ochiya, M. Olivier, A. Ortiz, L.A. Ortiz, X. Osteikoetxea, O. Ostergaard, M. Ostrowski, J. Park, D.M. Pegtel, H. Peinado, F. Perut, M.W. Pfaffl, D.G. Phinney, B.C. Pieters, D.S. Pink, E. Pisetsky, I. Pogge von Strandmann, I.K. Polakovicova, B.H. Poon, I. Powell, L. Prada, P. Pulliam, Quesenberry, A. Radeghieri, R.L. Raffai, S. Raimondo, J. Rak, M.I. Ramirez, G. Raposo, M.S. Rayyan, N. Regev-Rudzki, F. L. Ricklefs, P.D. Robbins, D.D. Roberts, S.C. Rodrigues, E. Rohde, S. Rome, K. M. Rouschop, A. Rughetti, A.E. Russell, P. Saa, S. Sahoo, E. Salas-Huenuleo, C. Sanchez, J.A. Saugstad, M.J. Saul, R.M. Schiffelers, R. Schneider, Schoyen, A. Scott, E. Shahaj, S. Sharma, O. Shatnyeva, F. Shekari, G.V. Shelke, A.K. Shetty, K. Shiba, P.R. Siljander, A.M. Silva, A. Skowronek, O.L. Snyder, R.P. Soares, B. W. Sodar, C. Soekmadji, J. Sotillo, P.D. Stahl, W. Stoorvogel, S.L. Stott, E. F. Strasser, S. Swift, H. Tahara, M. Tewari, K. Timms, S. Tiwari, R. Tixeira, M. Tkach, W.S. Toh, R. Tomasini, A.C. Torrecilhas, J.P. Tosar, V. Toxavidis, L. Urbanelli, P. Vader, B.W. van, Balkom, S.G. van der Grein, J. Van Deun, M.J. van Herwijnen, K. Van Keuren-Jensen, G. van Niel, M.E. van Royen, A.J. van Wijnen, M.H. Vasconcelos, I.J. Vechetti Jr., T.D. Veit, L.J. Vella, E. Velot, F.J. Verweij, B. Vestad, J.L. Vinas, T. Visnovitz, K.V. Vukman, J. Wahlgren, D.C. Watson, M. H. Wauben, A. Weaver, J.P. Webber, V. Weber, A.M. Wehman, D.J. Weiss, J. A. Welsh, S. Wendt, A.M. Wheelock, Z. Wiener, L. Witte, J. Wolfram, A. Xagorari, P. Xander, J. Xu, X. Yan, M. Yanez-Mo, H. Yin, Y. Yuana, V. Zappulli, J. Zarubova, V. Zekas, J.Y. Zhang, Z. Zhao, L. Zheng, A.R. Zheutlin, A.M. Zickler, P. Zimmermann, A.M. Zivkovic, D. Zocco, E.K. Zuba-Surma, Minimal information for studies of extracellular vesicles 2018 (MISEV2018): a position statement of the International Society for Extracellular Vesicles and update of the MISEV2014 guidelines, J. Extracell. Vesicles 7 (2018) 1535750, https://doi.org/10.1080/20013078.2018.1535750.

[23] A. Moller, R.J. Lobb, The evolving translational potential of small extracellular vesicles in cancer, Nat. Rev. Cancer 20 (2020) 697–709, https://doi.org/10.1038/s41568-020-00299-w.

[24] L. Gong, B. Chen, J. Zhang, Y. Sun, J. Yuan, X. Niu, G. Hu, Y. Chen, Z. Xie, Z. Deng, Q. Li, Y. Wang, Human ESC-sEVs alleviate age-related bone loss by rejuvenating senescent bone marrow-derived mesenchymal stem cells, J. Extracell. Vesicles 9 (2020) 1800971, https://doi.org/10.1080/20013078.2020.1800971.

[25] D. Hoffman-Kim, J.A. Mitchel, R.V. Bellamkonda, Topography, cell response, and nerve regeneration, Annu. Rev. Biomed. Eng. 12 (2010) 203–231, https://doi.org/10.1146/annurev-bioeng-070909-105351.

[26] S. Chen, H. Wang, V. Mainardi, G. Talò, A. McCarthy, J.V. John, M.J. Teusink, L. Hong, J. Xie, Biomaterials with structural hierarchy and controlled 3D nanotopography guide endogenous bone regeneration, Sci. Adv. 7 (2021), https://doi.org/10.1126/sciadv.abg3089.

[27] J.C. Doloff, O. Veiseh, R. de Mezerville, M. Sforza, T.A. Perry, J. Haupt, M. Jamiel, C. Chambers, A. Nash, S. Aghlara-Fotovat, J.L. Stelzel, S.J. Bauer, S.Y. Neshat, J. Hancock, N.A. Romero, Y.E. Hidalgo, I.M. Leiva, A.M. Munhoz, A. Bayat, B. M. Kinney, H.C. Hodges, R.N. Miranda, M.W. Clemens, R. Langer, The surface topography of silicone breast implants mediates the foreign body response in mice, rabbits and humans, Nat. Biomed. Eng. 5 (2021) 1115–1130, https://doi.org/10.1038/s41551-021-00739-4.

[28] C. Hu, C. Chu, L. Liu, C. Wang, S. Jin, R. Yang, S. Rung, J. Li, Y. Qu, Y. Man, Dissecting the microenvironment around biosynthetic scaffolds in murine skin wound healing, Sci. Adv. 7 (2021), https://doi.org/10.1126/sciadv.abf0787.

[29] M. Yao, S. Cheng, G. Zhong, J. Zhou, H. Shao, L. Ma, C. Du, F. Peng, Y. Zhang, Enhanced osteogenesis of titanium with nano-Mg(OH)2 film and A mechanism study via whole genome expression analysis, Bioact. Mater. 6 (2021) 2729–2741, https://doi.org/10.1016/j.bioactmat.2021.02.003.

[30] L. Bai, Y. Zhao, P. Chen, X. Zhang, X. Huang, Z. Du, R. Crawford, X. Yao, B. Tang, R. Hang, Y. Xiao, Targeting early healing phase with titania nanotube Arrays on tunable diameters to accelerate bone regeneration and osseointegration, Small 17 (2021), e2006287, https://doi.org/10.1002/smll.202006287.

[31] X. Fan, L. Zhu, K. Wang, B. Wang, Y. Wu, W. Xie, C. Huang, B.P. Chan, Y. Du, Stiffness-Controlled thermoresponsive hydrogels for cell harvesting with sustained mechanical memory, Adv. Healthc. Mater. 6 (2017), https://doi.org/10.1002/adhm.201601152.

[32] C. Yang, M.W. Tibbitt, L. Basta, K.S. Anseth, Mechanical memory and dosing influence stem cell fate, Nat. Mater. 13 (2014) 645–652, https://doi.org/10.1038/nmat3889.

[33] C.X. Li, N.P. Talele, S. Boo, A. Koehler, E. Knee-Walden, J.L. Balestrini, P. Speight, A. Kapus, B. Hinz, MicroRNA-21 preserves the fibrotic mechanical memory of mesenchymal stem cells, Nat. Mater. 16 (2017) 379–389, https://doi.org/10.1038/nmat4780.

[34] H. Liang, D. Zhao, X. Feng, L. Ma, X. Deng, C. Han, Q. Wei, C. Yang, 3D-printed porous titanium scaffolds incorporating niobium for high bone regeneration capacity, Mater. Des. 194 (2020), https://doi.org/10.1016/j.matdes.2020.108890.

[35] I. Lauria, T.N. Kutz, F. Boke, S. Rutten, D. Zander, H. Fischer, Influence of nanoporous titanium niobium alloy surfaces produced via hydrogen peroxide oxidative etching on the osteogenic differentiation of human mesenchymal stromal cells, Mater. Sci. Eng. C. Mater. Biol. Appl. 98 (2019) 635–648, https://doi.org/10.1016/j.msec.2019.01.023.

[36] X. Zhuang, B. Zhou, J. Ouyang, H. Sun, Y. Wu, Q. Liu, F. Deng, Enhanced MC3T3-E1 preosteoblast response and bone formation on the addition of nano-needle and nano-porous features to microtopographical titanium surfaces, Biomed. Mater. 9 (2014), 045001, https://doi.org/10.1088/1748-6041/9/4/045001.

[37] K.C. Popat, K.I. Chatvanichkul, G.L. Barnes, T.J. Latempa Jr., C.A. Grimes, T. A. Desai, Osteogenic differentiation of marrow stromal cells cultured on nanoporous alumina surfaces, J. Biomed. Mater. Res. 80 (2007) 955–964, https://doi.org/10.1002/jbm.a.31028.

[38] K. Cai, M. Lai, W. Yang, R. Hu, R. Xin, Q. Liu, K.L. Sung, Surface engineering of titanium with potassium hydroxide and its effects on the growth behavior of mesenchymal stem cells, Acta Biomater. 6 (2010) 2314–2321, https://doi.org/10.1016/j.actbio.2009.11.034.

[39] Z. Liao, S. Li, S. Lu, H. Liu, G. Li, L. Ma, R. Luo, W. Ke, B. Wang, Q. Xiang, Y. Song, X. Feng, Y. Zhang, X. Wu, W. Hua, C. Yang, Metformin facilitates mesenchymal stem cell-derived extracellular nanovesicles release and optimizes therapeutic efficacy in intervertebral disc degeneration, Biomaterials 274 (2021), https://doi.org/10.1016/j.biomaterials.2021.120850, 120850.

[40] Z. Xie, Y. Gao, C. Ho, L. Li, C. Jin, X. Wang, C. Zou, Y. Mao, X. Wang, Q. Li, D. Fu, Y. F. Zhang, Exosome-delivered CD44v6/C1QBP complex drives pancreatic cancer liver metastasis by promoting fibrotic liver microenvironment, Gut (2021), https://doi.org/10.1136/gutjnl-2020-323014.

[41] H.P. Bei, P.M. Hung, H.L. Yeung, S. Wang, X. Zhao, Bone-a-Petite: Engineering Exosomes towards Bone, Osteochondral, and Cartilage Repair Small (2021), e2101741, https://doi.org/10.1002/smll.202101741.

[42] A. Liu, D. Lin, H. Zhao, L. Chen, B. Cai, K. Lin, S.G. Shen, Optimized BMSC-derived osteoinductive exosomes immobilized in hierarchical scaffold via lyophilization for bone repair through Bmpr2/Acvr2b competitive receptor-activated Smad pathway, Biomaterials 272 (2021), https://doi.org/10.1016/j.biomaterials.2021.120718, 120718.

[43] M.A. Brennan, P. Layrolle, D.J. Mooney, Biomaterials functionalized with MSC secreted extracellular vesicles and soluble factors for tissue regeneration, Adv. Funct. Mater. 30 (2020), https://doi.org/10.1002/adfm.201909125.

[44] J. Liang, S. Gu, X. Mao, Y. Tan, H. Wang, S. Li, Y. Zhou, Endothelial cell morphology regulates inflammatory cells through MicroRNA transferred by extracellular vesicles, Front. Bioeng. Biotechnol. 8 (2020) 369, https://doi.org/10.3389/fbioe.2020.00369.

[45] F. Carfi Pavia, M.A. Di Bella, V. Brucato, V. Blanda, F. Zummo, I. Vitrano, C.M. Di Liegro, G. Ghersi, I. Di Liegro, G. Schiera, A 3Dscaffold of PLLA induces the morphological differentiation and migration of primary astrocytes and promotes the production of extracellular vesicles, Mol. Med. Rep. 20 (2019) 1288–1296, https://doi.org/10.3892/mmr.2019.10351.

[46] Y. Wan, M. Maurer, H.Z. He, Y.Q. Xia, S.J. Hao, W.L. Zhang, N.S. Yee, S.Y. Zheng, Enrichment of extracellular vesicles with lipid nanoprobe functionalized nanostructured silica, Lab Chip 19 (2019) 2346–2355, https://doi.org/10.1039/c8lc01359d.

[47] M. Liu, D. Wang, S. Gu, B. Tian, J. Liang, Q. Suo, Z. Zhang, G. Yang, Y. Zhou, S. Li, Micro/nano materials regulate cell morphology and intercellular communication by extracellular vesicles, Acta Biomater. 124 (2021) 130–138, https://doi.org/10.1016/j.actbio.2021.02.003.

[48] J. Wei, J. Shimazu, M.P. Makinistoglu, A. Maurizi, D. Kajimura, H. Zong, T. Takarada, T. Lezaki, J.E. Pessin, E. Hinoi, G. Karsenty, Glucose uptake and Runx2 synergize to orchestrate osteoblast differentiation and bone formation, Cell 161 (2015) 1576–1591, https://doi.org/10.1016/j.cell.2015.05.029.

[49] M. Rauner, M. Murray, S. Thiele, D. Watts, D. Neumann, Y. Gabet, L.C. Hofbauer, B. Wielockx, Epo/EpoR signaling in osteoprogenitor cells is essential for bone homeostasis and Epo-induced bone loss, Bone Res. 9 (2021) 42, https://doi.org/10.1038/s41413-021-00157-x.

[50] C. Dou, J. Li, J. He, F. Luo, T. Yu, Q. Dai, Y. Chen, J. Xu, X. Yang, S. Dong, Bone-targeted pH-responsive cerium nanoparticles for anabolic therapy in osteoporosis, Bioact. Mater. 6 (2021) 4697–4706, https://doi.org/10.1016/j.bioactmat.2021.04.038.

[51] K. Laperre, M. Depypere, N. van Gastel, S. Torrekens, K. Moermans, R. Bogaerts, F. Maes, G. Carmeliet, Development of micro-CT protocols for in vivo follow-up of mouse bone architecture without major radiation side effects, Bone 49 (2011) 613–622, https://doi.org/10.1016/j.bone.2011.06.031.

[52] D. Xu, Y. Wan, Z. Li, C. Wang, Q. Zou, C. Du, Y. Wang, Tailorable hierarchical structures of biomimetic hydroxyapatite micro/nano particles promoting endocytosis and osteogenic differentiation of stem cells, Biomater. Sci. 8 (2020) 3286–3300, https://doi.org/10.1039/d0bm00443j.

[53] L. Feng, D. Xue, E. Chen, W. Zhang, X. Gao, J. Yu, Y. Feng, Z. Pan, HMGB1 promotes the secretion of multiple cytokines and potentiates the osteogenic differentiation of mesenchymal stem cells through the Ras/MAPK signaling pathway, Exp. Ther. Med. 12 (2016) 3941–3947, https://doi.org/10.3892/etm.2016.3857.

[54] X. Liu, M. Chen, J. Luo, H. Zhao, X. Zhou, Q. Gu, H. Yang, X. Zhu, W. Cui, Q. Shi, Immunopolarization-regulated 3D printed-electrospun fibrous scaffolds for bone regeneration, Biomaterials 276 (2021), https://doi.org/10.1016/j.biomaterials.2021.121037, 121037.

[55] Z. Li, P. Wang, J. Li, Z. Xie, S. Cen, M. Li, W. Liu, G. Ye, G. Zheng, M. Ma, S. Wang, W. Yu, Y. Wu, H. Shen, The N(6)-methyladenosine demethylase ALKBH5 negatively regulates the osteogenic differentiation of mesenchymal stem cells through PRMT6, Cell Death Dis. 12 (2021) 578, https://doi.org/10.1038/s41419-021-03869-4.

[56] S. Iyer, E. Ambrogini, S.M. Bartell, L. Han, P.K. Roberson, R. de Cabo, R.L. Jilka, R. S. Weinstein, C.A. O'Brien, S.C. Manolagas, M. Almeida, FOXOs attenuate bone formation by suppressing Wnt signaling, J. Clin. Invest. 123 (2013) 3409–3419, https://doi.org/10.1172/JCI68049.

[57] S. Vermeulen, F. Honig, A. Vasilevich, N. Roumans, M. Romero, A. Dede Eren, U. Tuvshindorj, M. Alexander, A. Carlier, P. Williams, J. Uquillas, J. de Boer, Expanding biomaterial surface topographical design space through natural surface reproduction, Adv. Mater. (2021), e2102084, https://doi.org/10.1002/adma.202102084.

[58] L. Ye, J. Xu, J. Mi, X. He, Q. Pan, L. Zheng, H. Zu, Z. Chen, B. Dai, X. Li, Q. Pang, L. Zou, L. Zhou, L. Huang, W. Tong, G. Li, L. Qin, Biodegradable magnesium combined with distraction osteogenesis synergistically stimulates bone tissue regeneration via CGRP-FAK-VEGF signaling axis, Biomaterials 275 (2021), https://doi.org/10.1016/j.biomaterials.2021.120984, 120984.

[59] X. Xu, Y. Li, L. Wang, Y. Li, J. Pan, X. Fu, Z. Luo, Y. Sui, S. Zhang, L. Wang, Y. Ni, L. Zhang, S. Wei, Triple-functional polyetheretherketone surface with enhanced bacteriostasis and anti-inflammatory and osseointegrative properties for implant application, Biomaterials 212 (2019) 98–114, https://doi.org/10.1016/j.biomaterials.2019.05.014.

[60] Z. Sun, L. Ouyang, X. Ma, Y. Qiao, X. Liu, Controllable and durable release of BMP-2-loaded 3D porous sulfonated polyetheretherketone (PEEK) for osteogenic activity enhancement, Colloids Surf. B Biointerfaces 171 (2018) 668–674, https://doi.org/10.1016/j.colsurfb.2018.08.012.

[61] R. Ma, S. Tang, H. Tan, J. Qian, W. Lin, Y. Wang, C. Liu, J. Wei, T. Tang, Preparation, characterization, in vitro bioactivity, and cellular responses to a polyetheretherketone bioactive composite containing nanocalcium silicate for bone repair, ACS Appl. Mater. Interfaces 6 (2014) 12214–12225, https://doi.org/10.1021/am504409q.

[62] Chung-Sung Lee, Soyon Kim, Jiabing Fan, , Hee Sook Hwang, Tara Aghaloo, M. Lee, Smoothened agonist sterosome immobilized hybrid scaffold for bone regeneration, Sci. Adv. 6 (2020), https://doi.org/10.1126/sciadv.aaz7822.